

Transiently formed nucleus-to-cilium microtubule arrays mediate senescence initiation in a KIFC3-dependent manner

Received: 7 August 2023

Accepted: 4 September 2024

Published online: 12 September 2024

 Check for updatesJielu Hao Robichaud¹, Yingyi Zhang¹, Chuan Chen¹, Kai He¹, Yan Huang¹, Xu Zhang^{1,2}, Xiaobo Sun¹, Xiaoyu Ma¹, Gary Hardiman³, Ciaran G. Morrison⁴, Zheng Dong^{5,6}, Nathan K. LeBrasseur^{2,7,8}, Kun Ling¹ & Jinghua Hu^{1,9,10} ✉

Despite the importance of cellular senescence in human health, how damaged cells undergo senescence remains elusive. We have previously shown that promyelocytic leukemia nuclear body (PML-NBs) translocation of the ciliary FBF1 is essential for senescence induction in stressed cells. Here we discover that an early cellular event occurring in stressed cells is the transient assembly of stress-induced nucleus-to-cilium microtubule arrays (sinc-MTs). The sinc-MTs are distinguished by unusual polyglutamylation and unique polarity, with minus-ends nucleating near the nuclear envelope and plus-ends near the ciliary base. KIFC3, a minus-end-directed kinesin, is recruited to plus-ends of sinc-MTs and interacts with the centrosomal protein CENEXIN1. In damaged cells, CENEXIN1 co-translocates with FBF1 to PML-NBs. Deficiency of KIFC3 abolishes PML-NB translocation of FBF1 and CENEXIN1, as well as senescence initiation in damaged cells. Our study reveals that KIFC3-mediated nuclear transport of FBF1 along polyglutamylated sinc-MTs is a prerequisite for senescence induction in mammalian cells.

Cellular senescence is an irreversible growth arrest triggered by deleterious stimuli such as DNA damage, telomere shortening, oncogene activation, and metabolic dysfunction¹. Senescent cells release pro-inflammatory cytokines, chemokines, and other factors known as the senescence-associated secretory phenotype (SASP)². Although senescence is a natural part of life and can be helpful in maintaining tissue health and balance, when left unchecked it leads to the harmful release of SASP factors that increase the risk of cancer and age-related diseases³. Recent studies in rodent models have shown that clearing senescent cells using genetic or pharmacological methods can improve survival and overall health, making the targeting of

senescence a promising therapeutic approach to prevent or treat aging-related conditions and cancer^{4–7}.

Primary cilia are microtubule-based sensory organelles that protrude from the cell surface^{8,9}. Dysfunctions of cilia have been associated with dozens of rare genetic diseases, collectively known as ciliopathies^{10,11}. In our previous study of human cells exposed to irreparable stresses, we observed that FBF1, a component of transition fibers located at the base of primary cilia, unexpectedly translocates into the nucleus, and upregulates the formation of PML nuclear bodies (PML-NBs)¹², which are nuclear structures regulating stress-induced responses, including senescence^{13,14}.

¹Department of Biochemistry and Molecular Biology, Mayo Clinic, Rochester, MN, USA. ²Mayo Clinic Robert and Arlene Kogod Center on Aging, Mayo Clinic, Rochester, MN, USA. ³School of Biological Sciences, Institute for Global Food Security (IGFS), Queen's University Belfast, Belfast, Ireland. ⁴Centre for Chromosome Biology, School of Biological and Chemical Sciences, University of Galway, Galway, Ireland. ⁵Department of Cellular Biology and Anatomy, Medical College of Georgia at Augusta University, Augusta, GA, USA. ⁶Research Department, Charlie Norwood VA Medical Center, Augusta, GA, USA. ⁷Department of Physical Medicine and Rehabilitation, Mayo Clinic, Rochester, MN, USA. ⁸Department of Physiology and Biomedical Engineering, Mayo Clinic, Rochester, MN, USA. ⁹Mayo Clinic Robert M. and Billie Kelley Pirnie Translational Polycystic Kidney Disease Center, Mayo Clinic, Rochester, MN, USA. ¹⁰Division of Nephrology and Hypertension, Mayo Clinic, Rochester, MN, USA. ✉e-mail: hu.jinghua@mayo.edu

However, the mechanism by which the ciliary FBF1 is transported from the base of primary cilia to the nucleus in damaged cells remains unclear.

Microtubules (MTs) form the most important intracellular transport system, driven by motor proteins including members of the kinesin superfamily or dyneins. MTs are long polymers of $\alpha\beta$ -tubulin-dimer that are arranged in a polarized manner within the cell, with a dynamically growing plus-end and a comparatively stable minus end¹⁵. MTs emanate from ‘microtubule-organizing centres’ (MTOCs), or sites localize MT minus ends¹⁶. The highly organized MT network controls the directionality of motor proteins and facilitates the transportation of relevant cargo. Plus-end-directed kinesins move cargos away from the MTOC, whereas minus-end-directed dyneins move cargos towards the MTOC¹⁷. Despite the major MTOC in mammalian cells is the centrosome, alternative MTs nucleated from non-centrosomal MTOCs are also documented in different contexts¹⁶. The function of MTs is regulated by a variety of post-translational modifications (PTMs), such as polyglutamylation, polyglycylation, acetylation, and phosphorylation^{18–20}. A recent study observed an increase in MT stability in senescent cells due to enhanced α -tubulin acetylation, which suggests the importance of MT PTM in regulation of senescence²¹. However, if and how MT arrays reorganize in stressed cells and how they impact senescence responses remain largely unexplored.

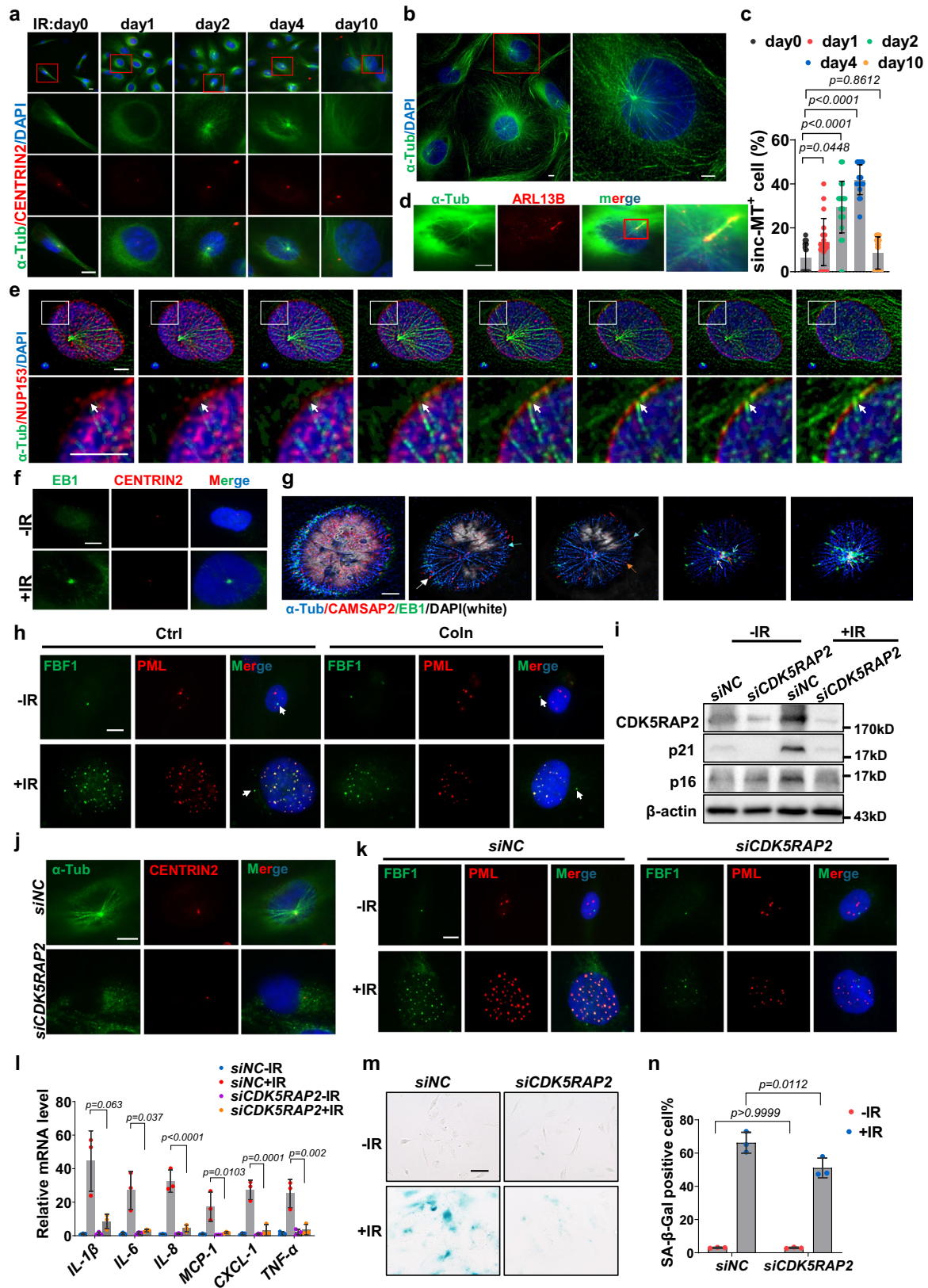
Here, we demonstrate that stressed human cells dynamically form a subset of noncanonical and heavily polyglutamylated stress-induced-nucleus-to-cilium microtubule arrays (sinc-MTs). Unlike conventional MTs nucleated around the centrosome or the basal body, sinc-MTs have minus ends nucleated near the nuclear envelope but plus ends projected to the basal body. Disruption of sinc-MTs or its polyglutamylation modification suppresses senescence by blocking the PML-NB translocation of FBF1. We further revealed that the minus-end-directed kinesin KIFC3 is recruited to plus ends of sinc-MTs at the ciliary base, and then facilitates the nuclear transport of FBF1 in stressed cells. Unbiased proximity labeling proteomics identified CENEXIN1, a centrosomal protein implicated in regulating the assembly of centriolar appendages^{22–24}, interacts with KIFC3 and co-translocates with FBF1 to PML-NBs. Consistently, deficiency of KIFC3 or CENEXIN1 completely disrupts nuclear translocation of FBF1 and senescence induction in stressed cells. Together, these findings demonstrate the physiological importance of an unconventionally polarized and polyglutamylated sinc-MTs in regulation of stress responses and highlight the minus-end-directed kinesin KIFC3 as the key motor in mediating nuclear translocation of senescence regulators along sinc-MTs. Our research thus provides seminal insights into how the direct communication between the primary cilium and the distant nucleus is achieved in stressed cells to initiate cellular senescence.

Results

Transiently assembled sinc-MTs promote cellular senescence

We previously discovered that exposure to irreparable stressors induces transient cilia biogenesis, followed by the nuclear translocation of the ciliary protein FBF1 to induce PML-NB-dependent senescence in stressed human cells¹². When studying irradiation (IR) treated human renal cortical tubular epithelial (RCTE) or human primary lung embryonic fibroblasts (IMR90) cells, we observed a subset of microtubule arrays transiently upregulate and form connections between the ciliary base and the nucleus (Fig. 1a, b, Supplementary Fig. 1a). We hereafter designate the newly formed subset of MT arrays in stressed cells as stress-induced nucleus-to-cilium microtubule arrays (sinc-MTs). After the treatment with IR, microtubules (MTs) undergo significant reorganization in stressed cells. Within one day after the IR treatment, we observed MT arrays reorganize around the nucleus. By day two, a distinct subset of nucleus-to-cilium microtubule arrays,

hereafter termed sinc-MTs, becomes evident. These sinc-MTs become predominant in damaged cells by day four. However, their presence gradually diminishes by day 10 as damaged cells enter a senescent state. (Fig. 1a–c, Supplementary Fig. 1a). Consistently, the formation of sinc-MTs, PML-NB translocation of FBF1, and upregulation of PML-NBs were also observed in chemotherapy (Doxorubicin)- or inflammatory (IL1 β) stressor-induced senescent cells (Supplementary Fig. 1f–j). Employing ARL13B as a ciliary marker, we found that sinc-MTs exhibited a close association with the ciliary base (Fig. 1d), and that the majority of sinc-MTs formed in ciliated cells (Supplementary Fig. 1b). Disruption of cilia formation through *shIFT88* treatment significantly impeded the formation of sinc-MTs (Supplementary Fig. 1c, d). By using the nuclear pore protein, NUP153, as a marker for the nuclear envelope, we found that sinc-MTs are in close proximity to the nuclear envelope (Fig. 1e, Supplementary Movie 1). We next examined NESPRIN1, a key player bridges the nucleoskeleton and the cytoskeleton²⁵. Notably, exposure to IR led to a substantial redistribution of NESPRIN1 to cytoplasmic puncta in RCTE cells. Nevertheless, we detected frequent colocalization between sinc-MTs and NESPRIN1 around the nuclear envelope (Supplementary Fig. 1e). MT plus-end-binding protein1 (EB1) regulates MT dynamics by capturing and stabilizing MT plus-ends^{26,27}. In normal cells, the basal body acts as the centrosomal MTOC to nucleate the minus ends of MT arrays. IR treatment leads to strong accumulation of EB1 near the ciliary base in RCTE cells (Fig. 1f). The coincidence of the assembly of sinc-MTs and the unusual ciliary recruitment of EB1 in stressed but not healthy cells suggest that sinc-MTs exhibit an unconventional polarity with minus-ends nucleated from the nuclear envelope, but plus-ends projected towards the ciliary base. To validate the polarity of sinc-MTs, we initially performed co-staining using microtubule plus-end marker, EB1, and CAMSAP2, an established microtubule minus-end marker²⁸. Using super-resolution confocal scanning from the nucleus to the ciliary base, we frequently observed that in the formed sinc-MTs, the plus-end marker EB1 associates with the ciliary base, while the minus-end marker CAMSAP2 is localized near the nuclear envelope on the same microtubule filament (Fig. 1g). To further confirm this, we employed live-cell imaging. In non-IR treated cells, we observed EB1 moving away from the ciliary base (Supplementary Movie. 2). However, in IR-treated cells, we frequently observed EB1 comets projecting into and embedding at the ciliary base, indicating the formation of unconventional polarized MTs (Supplementary Movie. 3). We further explored the localization of CDK5RAP2, a key player that interacts with the γ -tubulin ring complex (γ TuRC) to stimulate γ TuRC-dependent microtubule nucleation²⁹. Interestingly, CDK5RAP2 was recruited to the vicinity of the nuclear envelope following IR treatment but this IR-induced localization become absent in senescent cells, suggesting that IR induces nucleation of MT minus-ends from the proximity of the nuclear envelope (Supplementary Fig. 2a). To determine the significance of the transient formation of sinc-MTs is mediating senescence induction, we employed colchicine to disrupt sinc-MT assembly. As anticipated, colchicine treatment completely abolished MT arrays in RCTE cells (Supplementary Fig. 1k). Notably, colchicine treatment in stressed cells resulted in a noteworthy suppression of senescence and PML-NB-associated phenotypes, including the PML-NB translocation of FBF1, the upregulation of PML-NBs, the nucleus size, the *PML* gene transcription, the production of type I interferon (IFN β), and the activity of Senescence-Associated β -galactosidase (SA- β -gal) (Fig. 1h, Supplementary Fig. 1l–q). To further confirm if stress-induced MT reorganization is critical for senescence induction, we depleted *CDK5RAP2* in RCTE and IMR90 cells, respectively. As expected, *CDK5RAP2* deficiency disrupted the assembly of sinc-MTs (Fig. 1j), inhibited the nuclear translocation of FBF1 (Fig. 1k), abolished EB1 recruitment, reduced the PML-NBs upregulation, the nucleus size, the *PML* gene transcription, and the IFN β production in IR-treated cells (Supplementary Fig. 2b–f, j, k). Consistently, *CDK5RAP2*-depleted



cells showed significantly reduced SA-β-Gal activity (Fig. 1m, n, Supplementary Fig. 2g), suppressed expression of SASP genes (Fig. 1l, Supplementary Fig. 2h, i) and molecular senescence markers (p16^{INK4A} and p21^{CIP1}) (Fig. 1i). Collectively, these results suggest that uncanonically polarized sinc-MTs are crucial for initiating cellular senescence in human cells exposed to irreparable stresses.

Polyglutamylation of sinc-MTs is essential for senescence induction

Tubulin PTMs add “tubulin code” to confer the dynamic, functional diversity of diverse MT arrays. The sinc-MTs are highly polyglutamylated (Fig. 2a, b, Supplementary Fig. 3a), but not acetylated (Supplementary Fig. 3b) in IR-treated human cells. 3D

Fig. 1 | Irreparable stress induces transient assembly of sinc-MTs that promote cellular senescence in human cells. **a** Immunofluorescent images of sinc-MTs in IR-treated RCTE cells. α -tubulin (green) labels MTs. CENTRIN2 (red) labels the ciliary base. Scale bar, 10 μ m. **b** Stacked z-steps deconvolution image of RCTE cells exposed to IR on day 2 using α -tubulin (green) labeling MTs. Scale bar, 10 μ m. **c** Quantification of sinc-MTs-positive cells, calculated as the ratio of positive cells to the total number of cells ($n = 20$ fields, 10–20 cells per field). **d** Immunofluorescence showing sinc-MTs and the cilium in IR-treated RCTE cells. α -tubulin (green) labels MTs. ARL13B (red) labels primary cilium. Scale bar, 10 μ m. **e** Confocal z-stack of IR-treated RCTE cells, with arrows pointing at sinc-MTs (α -tubulin, green) near the nuclear envelope (NUP153, red). Scale bar, 5 μ m. **f** Immunofluorescence of sinc-MTs plus-end binding protein EB1 (green) near the ciliary base (CENTRIN2, red) in IR-treated RCTE cells. Scale bar, 10 μ m. **g** Confocal z-stack images in IR-treated RCTE cells using antibodies against α -tubulin (blue), CAMSAP2 (red), and EB1 (green). Arrows indicate the minus- and plus-ends of sinc-

MT filaments. Scale bar, 5 μ m. **h** Localization PML (red) and FBF1 (green) in IR-treated RCTE cells with or without colchicine treatment. Arrows indicate the ciliary base. Scale bar, 10 μ m. **i** Western blot of CDK5RAP2 and senescence markers in control or *siCDK5RAP2* RCTE cells 10 days post-IR. **j** Immunofluorescence of sinc-MTs (α -tubulin, green) in IR-treated control or *siCDK5RAP2* RCTE cells. CENTRIN2 (red) labels the ciliary base. Scale bar, 10 μ m. **k** Immunostaining of PML-NBs (red) and FBF1 (green) in IR-treated control or *siCDK5RAP2* RCTE cells. Scale bar, 10 μ m. Relative mRNA level of SASP genes (**l**), SA- β -gal staining (**m**), quantitation of the percentage of SA- β -gal-positive cells ($n = 3$ independent experiments, 6–8 fields per experiment, 100–200 cells per field) (**n**) in control or *siCDK5RAP2* RCTE cells 10 days post-IR. Scale bar, 50 μ m. All results from $n = 3$ independent experiments. Data are the mean \pm SEM. One-way ANOVA was used analyzing (**c**, **l**, **n**). Three experiments were repeated independently with similar results (**a**, **b**, **d**–**k**). Source data are provided as a Source Data file.

surface-rendering reconstruction of serial images obtained from Super-resolution structured illumination microscope (SIM) further confirmed that the polyglutamylated sinc-MTs connect between the nuclear envelope and the ciliary base (Fig. 2c, Supplementary Movie. 4). Consistently, SIM microscopy confirmed that EB1 strongly labels the ends of sinc-MTs near the ciliary base in IR-treated cell (Fig. 2d). Among all the PTMs of MTs, polyglutamylation occurs in cilia but not in other MT structures in healthy mammalian non-neural cells^{30–32}. It is important to mention that polyglutamylation on sinc-MTs exhibits a puncta-like pattern, whereas the modification along the axoneme occurs continuously. We previously reported that tubulin glutamylases TLL5 and TLL6 mediate axoneme polyglutamylation in mammalian cilia³³. Of note, in IR-treated cells, we observed that YFP-tagged TLL5 and TLL6 accumulate specifically near the ciliary base (Fig. 2e, Supplementary Fig. 3c). Knockdown of *TLL5* efficiently abolished the polyglutamylation modification along sinc-MTs (Fig. 2f, g), and resulted in significantly reduced senescence responses, as indicated by decreased SA- β -gal activity (Fig. 2h, i, Supplementary Fig. 3d), and also reduced expression of SASP genes (Fig. 2j, k, Supplementary Fig. 3g, j), the *PML* gene upregulation (Supplementary Fig. 3h), the IFN β production (Supplementary Fig. 3i), and the nucleus size (Supplementary Fig. 3k). Furthermore, knockdown of *TLL5* significantly inhibited PML-NB translocation of FBF1 which could be restored by *TLL5* re-expression (Fig. 2l, m, Supplementary Fig. 3e). Similarly, depletion of *TLL6* also reduced SA- β -Gal activity and SASP gene expression in IR-treated cells (Supplementary Fig. 3f, l–o). However, the simultaneous suppression of *TLL5* and *TLL6* did not yield additive effects on cells following exposure to IR (Supplementary Fig. 3q, r). This outcome is probably attributed to the crucial roles played by *TLL5* and *TLL6* in regulating distinct steps of glutamylation modification. Tubulin polyglutamylation was recently shown to direct another tubulin modification, detyrosination³⁴. To investigate whether the impact of synchronized microtubule polyglutamylation on senescence is linked to detyrosination modification, we examined the detyrosination levels of sinc-MTs. We did not observe detyrosination along sinc-MTs (Supplementary Fig. 3s). Additionally, not like *TLL5*, the transcriptional level of detyrosinase *VASH1* and *VASH2* did not respond to IR treatment (Supplementary Fig. 3p). These data suggest that polyglutamylation modification of sinc-MTs is crucial for inducing senescence in damaged cells.

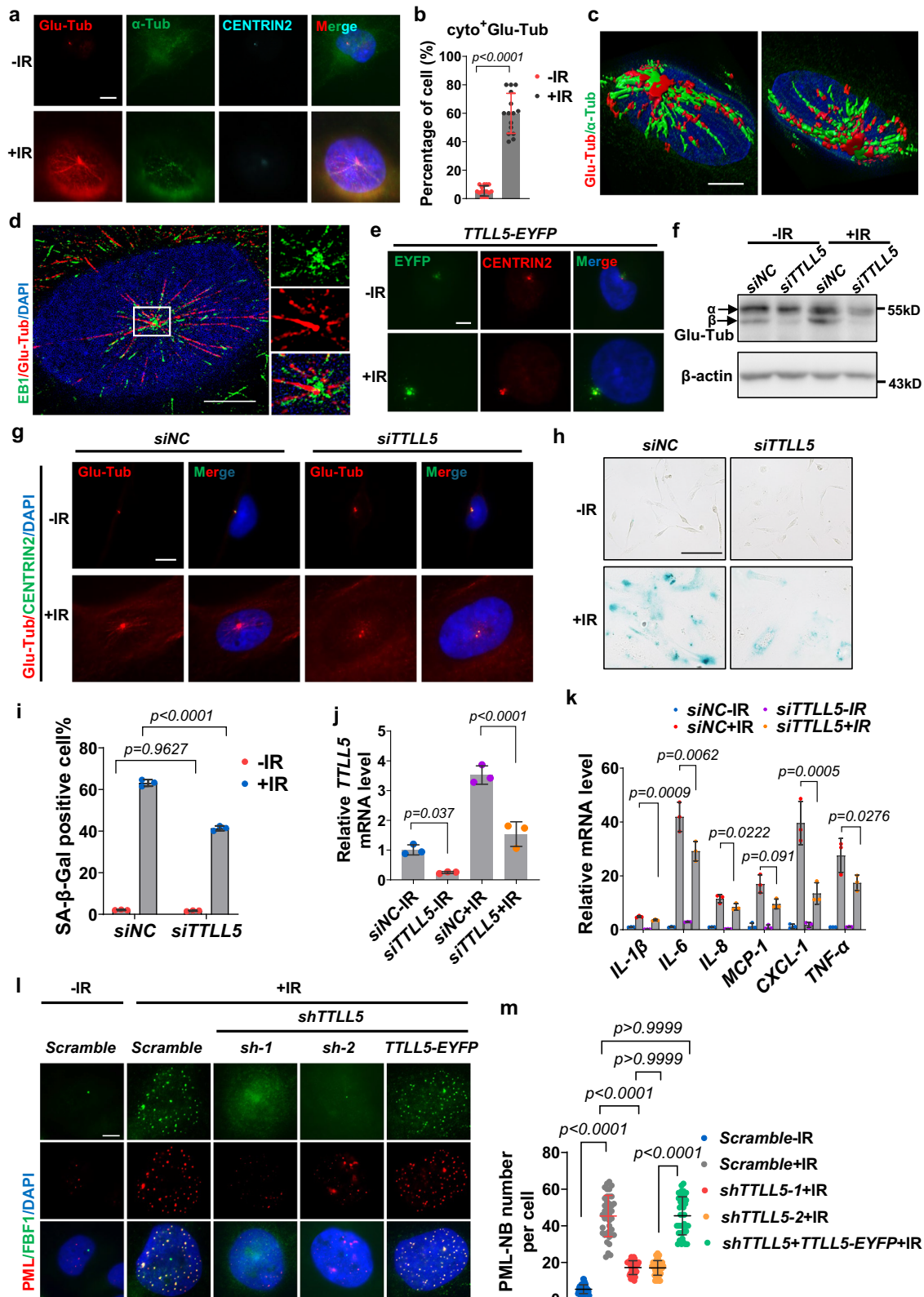
Minus-end-directed kinesin KIFC3 uses sinc-MTs to induce senescence

The unique polarity of sinc-MTs implies a minus-end-directed motor that transports FBF1 to the nucleus, triggering cilia-mediated cellular senescence. Of note, the absence of the cytoplasmic dynein does not affect senescence responses in cells exposed to IR (Supplementary Fig. 4a, b). Except for the cytoplasmic dynein, the C-terminal kinesins in the kinesin-14 family are noncanonical kinesins that can move cargos

towards MT minus-ends³⁵. We thus investigated two kinesin-14 members KIFC2 and KIFC3. KIFC2 did not exhibit any cilia-related localization (Supplementary Fig. 4c), whereas KIFC3 was significantly upregulated in senescent cells and found to label the ciliary base, with its ciliary localization further enhanced after IR treatment (Fig. 3a–c). Through serial section analysis of SIM images, we observed a strong association between KIFC3 and polyglutamylated sinc-MTs, with the highest signal enriched around plus-ends of sinc-MTs in IR-treated cells (Fig. 3d, e). To validate the mobility of KIFC3, we generated a StayGold-tagged variant of KIFC3. Live-cell imaging demonstrated a robust accumulation of StayGold-KIFC3 at the ciliary base upon IR exposure, with frequent movements detected away from the ciliary base (Supplementary Movie. 5). This observation suggests that the MT track along which KIFC3 moves has plus-ends in close proximity to the ciliary base. Disrupted polyglutamylation of sinc-MTs by *siTLL5* treatment abolished the association between KIFC3 with sinc-MT arrays (Fig. 3f), suggesting that KIFC3 recognizes and/or moves along sinc-MTs via a polyglutamylation-dependent manner. To determine whether KIFC3 is involved in regulating cellular senescence, we knocked down *KIFC3* in both RCTE and IMR90 cells. *KIFC3* deficiency strongly reduced senescence responses, as demonstrated by assessing molecular senescence markers, SA- β -gal activity, and SASP gene expression (Fig. 3g–j, Supplementary Fig. 4d), and resulted in significantly decrease in *PML* gene upregulation and IFN β production (Supplementary Fig. 4e–g). These findings suggest that the minus-end-directed motor protein KIFC3 utilizes the unconventionally polarized sinc-MTs to induce senescence responses in stressed human cells.

KIFC3 interactor CENEXIN1 co-translocates with FBF1 to PML-NBs

We next explored whether FBF1 acts as a cargo for KIFC3. However, co-immunoprecipitation experiments revealed no physical interaction between KIFC3 and FBF1 (Fig. 4a). Therefore, we hypothesized that an intermediate protein might tether FBF1 to KIFC3 during transport along sinc-MTs. To identify this player, we employed BioID (proximity-dependent biotin identification) proteomics to label and catalog FBF1's interactome³⁶. We reasoned that the intermediate protein, to enable KIFC3-mediated transport of FBF1 along sinc-MTs towards the nucleus, should be enriched near the plus-ends of sinc-MTs, specifically the ciliary base, and might even co-transport with FBF1 to the nucleus. By characterizing the localization of cilia-related candidates of FBF1 interactome in senescent cells, we discovered the centrosomal protein CENEXIN1 (coded by the *ODF2* gene) as a promising candidate (Supplementary Table. S1). CENEXIN1 and FBF1 were found to associate with each other, with their association significantly upregulated after IR treatment (Fig. 4b, c). Importantly, CENEXIN1 and FBF1 co-distribute to PML-NB in IR-treated cells (Fig. 4g, Supplementary Fig. 5a). Moreover, utilizing APEX2-based Bio-ID³⁷ analyses with CENEXIN1 as the prey, we identified KIFC3 as part of the CENEXIN1 interactome



(Supplementary Table. S2). We confirmed the interaction between CENEXIN1 and KIFC3 by co-IP and reciprocal IP in IR-treated cells (Fig. 4d–f). Using SIM microscopy and bimolecular fluorescence complementation (BiFC) assay, we found that CENEXIN1 closely associates with KIFC3, surrounded by EB1-labeled microtubule plus-ends, at the ciliary base in stressed cells (Fig. 4h, Supplementary Fig. 5b). Collectively, our evidence strongly suggests that centrosomal

protein CENEXIN1 interacts with KIFC3 and co-translocates with FBF1 to PML-NBs in IR-treated cells.

Nuclear translocation of CENEXIN1-FBF1 requires KIFC3 motor
KIFC3 contains a N-terminal coiled-coil domain serving as cargo-binding domain and a C-terminal kinesin motor domain. We generated two truncated KIFC3 mutants, a KIFC3^{DN} (dominant negative) without

Fig. 2 | Polyglutamylation of sinc-MTs is required for DNA damage-induced senescence. Immunofluorescence images showing the polyglutamylation (labeled with GT335 antibody, red) of sinc-MTs (**a**) and quantitation of sinc-MT-positive cells ($n = 15$ fields, 10–25 cells per field) (**b**) in RCTE cells with or without IR exposure. MTs labeled with α -tubulin (green), and the ciliary base labeled with CENTRIN2 (cyan). Scale bar, 10 μm . **c** 3D surface-rendering reconstruction of serial sections of SIM images showing the polyglutamylated sinc-MTs between the nuclear envelope and the ciliary base in IR-treated RCTE cells. Glutamylated tubulin (red) and α -tubulin (green) were immunostained by antibodies, respectively. Scale bar, 10 μm . **d** Super-resolution SIM images of polyglutamylated sinc-MTs (red) with plus-end labeled with EB1 (green) in IR-treated RCTE cells. Scale bar, 10 μm . **e** Localization of EYFP-tagged TLL5 (green) in RCTE cells with or without IR exposure. CENTRIN2 (red) labels the ciliary base. Scale bar, 10 μm . **f** Western blot of glutamylated tubulins in control or *siTLL5* RCTE cells with or without IR exposure.

g Immunofluorescence images of polyglutamylated sinc-MTs (red) in control or *siTLL5* RCTE cells with or without IR exposure. CENTRIN2 (green) labels the ciliary base. Scale bar, 10 μm . **h** SA- β -gal staining (**h**), quantitation of the percentage of SA- β -gal-positive cells ($n = 3$ independent experiments, 6–8 fields per experiment with 100–200 cells per field) (**i**), relative mRNA levels of *TLL5* (**j**), and expression of SASP genes (**k**) in control or *siTLL5* RCTE cells at day 10 after IR exposure. Scale bar, 50 μm . Results from $n = 3$ independent experiments. Immunofluorescence images of PML-NBs (red) translocation of FBF1 (green) (**l**) and quantitation of PML-NBs numbers per cell ($n = 40$ cells) (**m**) in control or *shTLL5* IR-treated RCTE cells re-expressing EYFP-TLL5. Scale bar, 10 μm . Data are the mean \pm SEM. Two-tailed Unpaired Student's *t* test was used for analysis in (**b**). One-way ANOVA analysis was employed for (**i–k**, **m**). Three experiments were repeated independently with similar results (**d–g**). Source data are provided as a Source Data file.

the motor domain and a KIFC3^{AN} lacking cargo-binding domain (Fig. 5a). Consistent with our hypothesis that CENEXIN1 is a cargo of KIFC3, CENEXIN1 was co-immunoprecipitated with either WT or KIFC3^{DN}, however, we cannot completely exclude the possibility of interaction with KIFC3^{AN} due to its problematic expression (Fig. 5b, Supplementary Fig. 6a). Interesting, only the motorless KIFC3^{DN} but not the KIFC3^{AN} recapitulates the ciliary localization pattern of WT KIFC3 (Fig. 5c), indicating the ciliary recruitment of KIFC3 is solely dependent on its cargo binding capacity but not its motor activity. We further investigated whether the motor activity of KIFC3 is required for the nuclear translocation of the CENEXIN1-FBF1 complex. Although both localizing to the ciliary base, only re-expression of WT KIFC3, but not KIFC3^{DN} rescued the PML-NBs translocation of CENEXIN1 and FBF1 and PML-NBs upregulation in IR-treated *shKIFC3* RCTE cells (Fig. 5d, e). On the other hand, overexpression of the motorless KIFC3^{DN} in WT cells exhibited dominant negative impact on IR-induced PML-NBs translocation of CENEXIN1, PML-NBs upregulation, and SA- β -gal activity (Fig. 5f–h). To further confirm the motor activity of KIFC3 is critical for cilia-mediated senescence induction, we trapped exogenously expressed KIFC3 to subdistal appendages of the basal body at ciliary base by fusing it with a CEP-170C tag¹². Ciliary-trapped CEP170-KIFC3 hinders its capacity to facilitate the translocation of CENEXIN1 and FBF1 to PML-NBs, as well as the increase in PML-NBs observed in IR-treated *shKIFC3* RCTE cells (Fig. 5i, Supplementary Fig. 6b–d). These results imply that the nuclear translocation of CENEXIN1-FBF1 complex and senescence induction depends on the motor activity of KIFC3.

CENEXIN1 but not ODF2 regulates PML-NB translocation of FBF1

Similar to stress-induced FBF1 upregulation, we observed an increase in CENEXIN1 level in IR-treated cells (Fig. 6a). Interestingly, the upregulation of CENEXIN1 during senescence progression occurred approximately two days earlier than the upregulation of FBF1 (Fig. 6a), suggesting a crucial role for CENEXIN1 in regulating senescence induction. The *ODF2* gene encodes at least nine isoforms, including the major long isoform CENEXIN1 and the short isoform ODF2 (iso6)²⁴. To distinguish the roles of CENEXIN1 and the shorter ODF2 isoform in senescence regulation, we overexpressed NeonGreen (NG)-tagged CENEXIN1 or ODF2 (iso6). Only NG-tagged CENEXIN1, but not ODF2 (iso6), localized specifically to the ciliary base in non-senescent cells and translocated to the nucleus in senescent cells (Fig. 6b). Additionally, APEX2-tagged CENEXIN1 also faithfully translocated to PML-NBs after IR treatment (Fig. 6c). Knockdown of *CENEXIN1* disrupted PML-NBs translocation of FBF1 and PML-NBs upregulation in senescent cells (Fig. 6d, e, Supplementary Fig. 7a). We further used CRISPR/Cas9 to engineer both *CENEXIN1* and *ODF2* knockout RCTE cells. As expected, the knockout of *CENEXIN1* disrupted the PML-NBs translocation of FBF1 and the upregulation of PML-NBs in IR-treated cells, which could be rescued by re-expression of CENEXIN1 but not ODF2 (iso6) (Fig. 6f, g). Interestingly, while FBF1 deficiency impaired the upregulation of PML-NBs, as well as *PML* and *IFN β* gene transcription

(Supplementary Fig. 7b–f) it does not affect the nuclear translocation of CENEXIN1. However, in FBF1-deficient cells, a notable proportion of nuclear-translocated CENEXIN1 forms foci that are independent of PML-NBs (Supplementary Fig. 7g, h), indicating that while CENEXIN1 is essential for the nuclear translocation of FBF1, FBF1 is not required for the nuclear translocation but rather for the proper PML-NB recruitment of CENEXIN1 under stress conditions. Consistent with our previous discovery that primary cilia are required for PML-NBs translocation of FBF1 in stressed IMR-90 cells¹², cilia ablation by *shIFT88* treatment also blocked the nuclear translocation of CENEXIN1 (Supplementary Fig. 7i) and senescence responses (Supplementary Fig. 7j, k).

CENEXIN1 deficiency abolishes senescence induction

Lastly, we investigated the impact of CENEXIN1 deficiency on cellular senescence. *CENEXIN1* depletion led to reduced SA- β -Gal activity, decreased expression of SASP genes, and lower levels of senescence markers but increased apoptosis in response to irreparable stresses (Fig. 7a–d, Supplementary Fig. 8a–d, g). Consistent with our findings on the nuclear translocation of FBF1, only re-expression of CENEXIN1, but not ODF2 (iso6), was able to rescue senescence responses (Fig. 7e, f, Supplementary Fig. 8e, f). Furthermore, similar results were observed when investigating the role of CENEXIN1 in regulating IL1 β -induced senescence. Knockdown of *CENEXIN1* resulted in a significantly reduced senescence responses, as evidenced by decreased SA- β -Gal activity (Fig. 7g, h) and SASP gene expression (Fig. 7i) in IL1 β -treated cells. Collectively, our data suggest that CENEXIN1, but not the shorter isoform encoded by *ODF2*, plays a pivotal role in regulating cellular senescence. Our data suggest that CENEXIN1 plays a general role in regulating cellular senescence, while the shorter isoform encoded by *ODF2* does not have a significant impact on this process.

Discussion

Despite the widely recognized role of the primary cilium as the cellular “sensory antenna,” the direct communication between this surface structure and the nucleus, which serves as the cell’s central signaling hub, remains poorly understood. This study uncovers the mechanistic details of a crucial function of sinc-MTs in directly transmitting stress-induced signals from the primary cilium to the nucleus, thereby initiating senescence in stressed cells (Fig. 7j). Sinc-MTs, characterized by their unconventional polarization and their association with the minus-end-directed kinesin KIFC3, distinguish themselves from other microtubule-dependent cellular trafficking mechanisms. This unique configuration enables efficient transmission of limited signals generated by a small, solitary cilium to the nucleus. By revealing the role of sinc-MTs in this process, our study addresses a significant gap in our understanding of cellular signaling pathways and provides fresh insights into how the primary cilium communicates with the nucleus to regulate cellular responses to stress conditions. Except for FBF1 and CENEXIN1, some ciliopathy

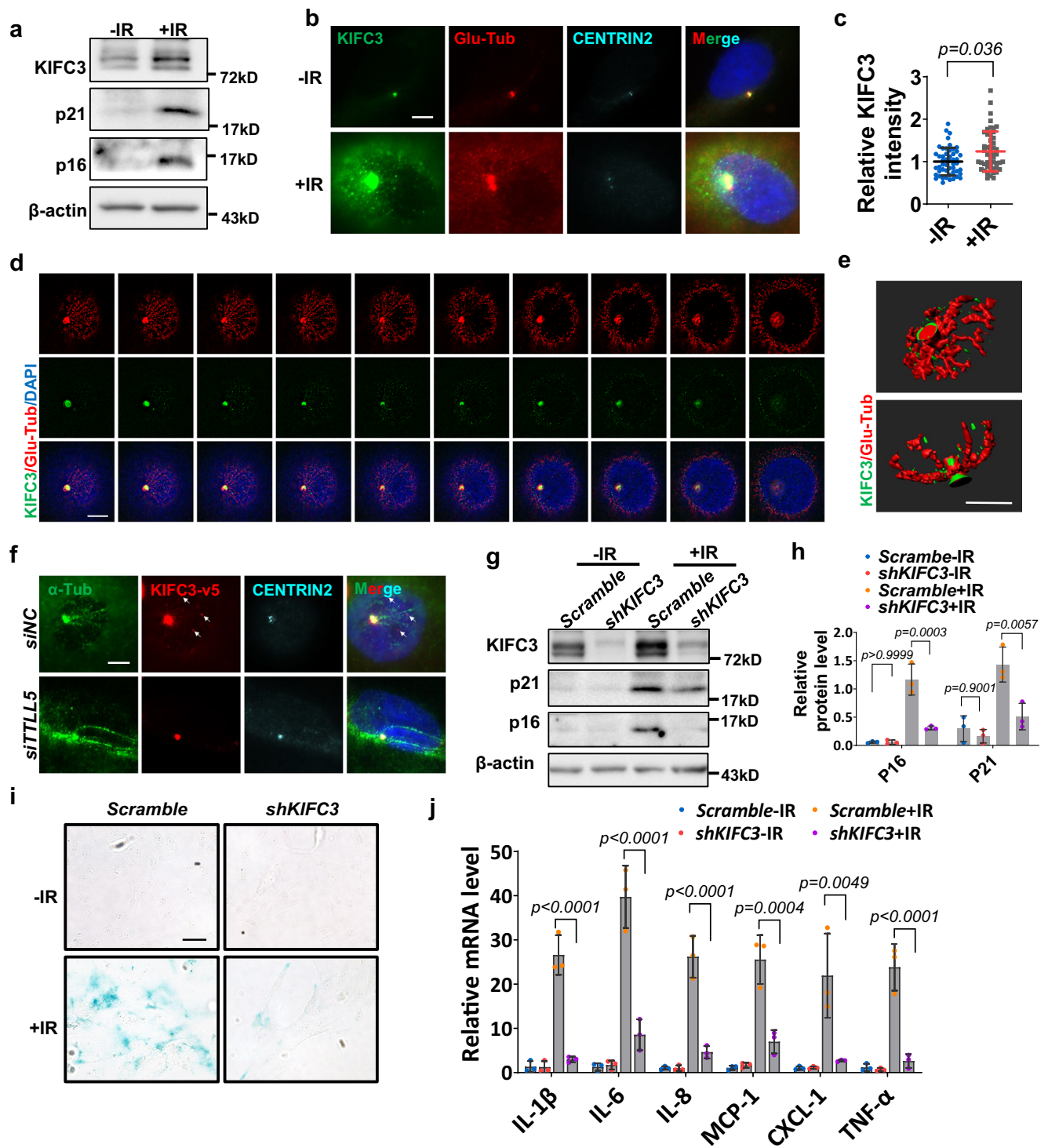


Fig. 3 | Minus-end-directed kinesin KIFC3 associates with sinc-MTs to mediate senescence induction. **a** Western blot detecting KIFC3 and senescence markers in RCTE cells with or without IR exposure. Three experiments were repeated independently with similar results. Immunofluorescent images showing KIFC3 (green) and polyglutamylated sinc-MTs (labeled with GT335 antibody, red) (**b**) and relative intensity of KIFC3 (**c**) in RCTE cells with or without IR exposure. CENTRIN2 (cyan) labels the ciliary base. $n = 50$ cells. Scale bar, 10 μm . SIM series section (**d**) and 3D surface-rendering reconstruction (**e**). Scale bar, 10 μm . Localization of KIFC3 (green) along polyglutamylated sinc-MTs (red) in RCTE cells exposed to IR.

f Immunofluorescence images showing KIFC3 and sinc-MTs (labeled with α -tubulin) in control or *siTLL5* RCTE cells after IR exposure. CENTRIN2 labels the ciliary base. Scale bar, 10 μm . Western blot of senescence markers (**g**), quantitation of relative protein levels of senescence markers (**h**), SA- β -gal staining (**i**), relative mRNA level of SASP genes (**j**) in control or *shKIFC3* RCTE cells at day 10 after IR exposure. Scale bar, 50 μm . All results from $n = 3$ independent experiments. Data are the mean \pm SEM. Statistical significance was determined using one-way ANOVA. Three experiments were repeated independently with similar results (**d–f**). Source data are provided as a Source Data file.

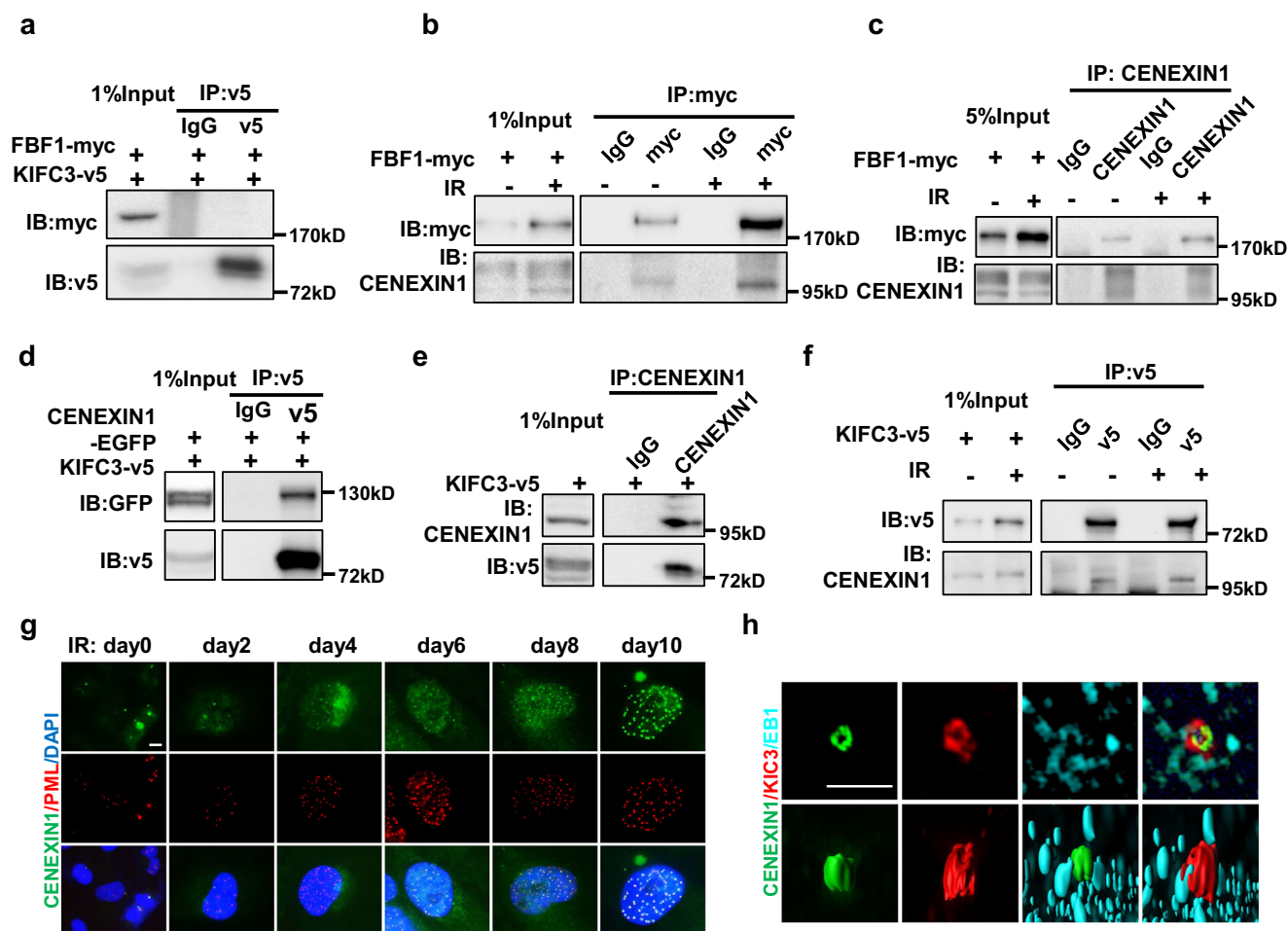


Fig. 4 | Centrosomal protein CENEXIN1 interacts with KIFC3 and co-translocates with FBF1 to PML-NBs in IR-treated cells. **a** Immunoprecipitation showing no interaction between V5-tagged KIFC3 and Myc-tagged FBF1 when overexpressed in 293 T cells. **b, c** Immunoprecipitation of endogenous CENEXIN1 with Myc-tagged FBF1 in IR-treated RCTE cells. **d** V5-tagged KIFC3 immunoprecipitates with EGFP-tagged CENEXIN1 when overexpressed in 293 T cells. **e, f** Endogenous CENEXIN1 immunoprecipitates with V5-tagged KIFC3 in control or

IR-treated RCTE cells. **g** Immunofluorescence images showing PML-NBs translocation of CENEXIN1 (green) in IR-treated RCTE cells. PML (red) labels the PML-NBs. Scale bar, 10 μ m. **h** 3D surface-rendering reconstruction of SIM section images showing the spatial relationship among CENEXIN1 (green), KIFC3 (red), and EB1 (cyan) labeled plus-ends of sinc-MTs at ciliary base in IR-treated RCTE cells. Scale bar, 10 μ m. Three experiments were repeated independently with similar results (**a–h**). Source data are provided as a Source Data file.

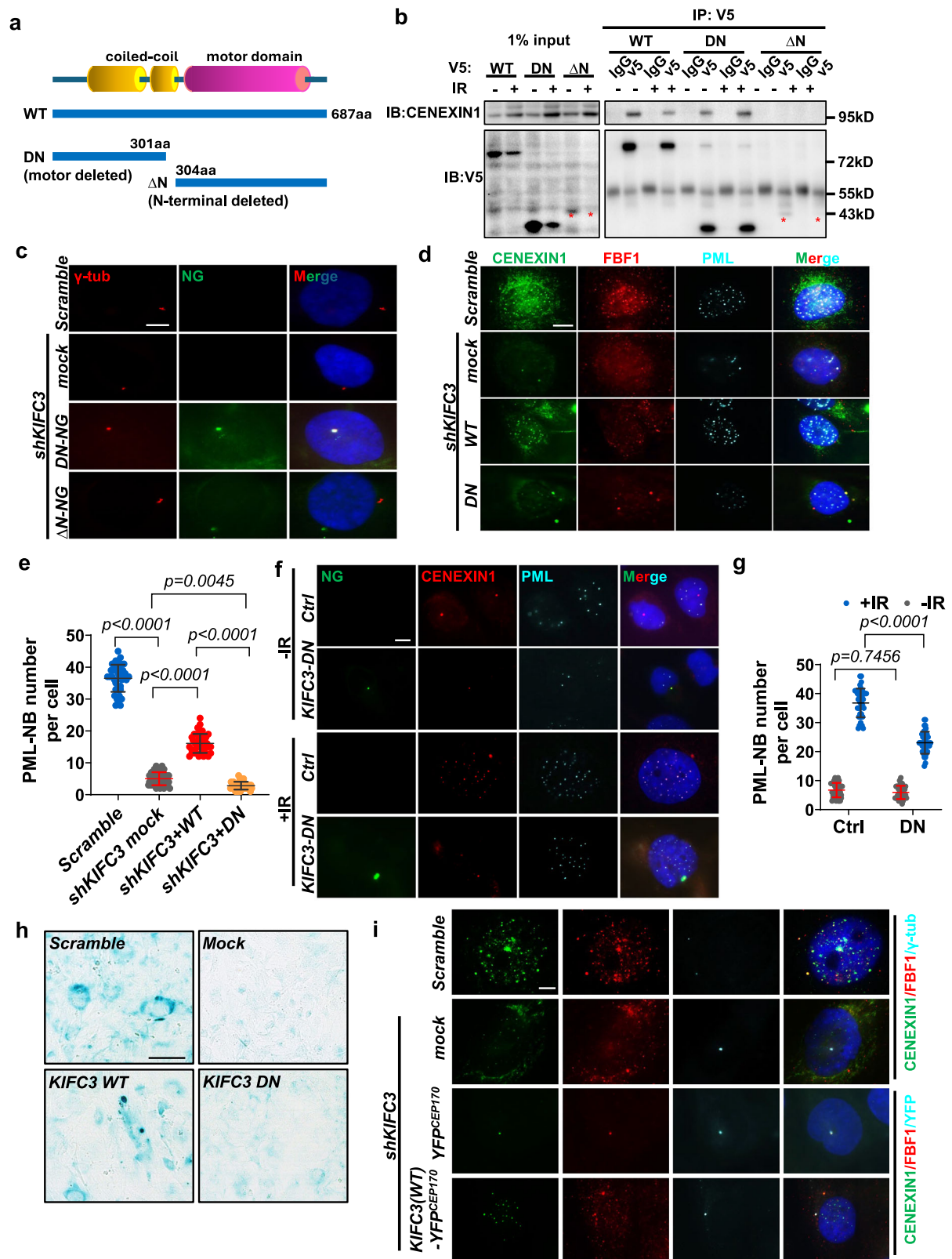
proteins, such as Joubert syndrome protein ZFN423, and Nephroptosis proteins CEP164 and NPHP10, relocate to unknown nuclear foci to regulate DNA damage responses^{38,39}. It would be interesting to investigate whether other stress-induced translocation of ciliary regulators also relies on sinc-MTs.

PTMs of MTs, such as polyglutamylation, can influence their mechanical properties and interactions with microtubule-associated proteins (MAPs), including motors, adaptors, and enzymes, ultimately affecting MT functions. Polyglutamylation is primarily observed in the axoneme and neuron axons but not in other MT structures^{30–32}. Microtubule polyglutamylation is a reversible process coordinated by nine tubulin tyrosine ligase-like (TLL) glutamylases^{40,41} and six cytoplasmic carboxyl peptidase deglutamylases⁴². The regulatory pathways and physiological importance of microtubule polyglutamylation are not clear. While our data show that polyglutamylation modification of MTs is crucial for selective nucleus translocation of senescence regulators, how polyglutamylated MTs regulate KIFC3 activity during senescence remains unknown. We previously show that impaired polyglutamylation has a subtle effect on axoneme stability³³. Although reported MT structures recognized by KIFC3 do not require polyglutamylation regulation⁴³, the absence of polyglutamylation along sinc-MTs might also affect the stability, and indirectly impair microtubule-bound KIFC3. Alternatively, molecular readers

recognizing polyglutamylated sinc-MTs may recruit, stabilize, or enhance KIFC3 mobility in senescence regulation. Further, the unique polyglutamylation modification of sinc-MTs suggests that enzymes/regulators involved in polyglutamylation regulation could be promising targets for developing senolytic strategies.

The use of primary fibroblast cells in most senescence studies as in vitro cell models has left gaps in our understanding of how stress conditions trigger the senescence response in different cell types. Among the different senescence-associated diseases, it has been established that senescent renal epithelia play a central role in the chronic progression and regeneration after kidney injury⁴⁴. Through our research, we have revealed the complex mechanisms that govern the transportation of cellular signaling molecules through sinc-MTs during the initiation stage of cellular senescence in human renal epithelial cells. Our findings not only provide a substantial advancement in our comprehension of how the primary cilium regulates the initiation of senescence in injured renal epithelial cells and its contribution to the transition from acute kidney injury (AKI) to chronic kidney disease but also highlight a potential therapeutic strategy to hinder the progression of detrimental senescence-associated kidney diseases in AKI patients.

So far, there have been at least 35 rare genetic disorders, primarily birth defects, that are known as ciliopathies, which collectively impact



pattern formation and homeostasis of most human organs and tissues^{10,11}. Despite their significance, the in vivo functions of most proteins associated with ciliopathies are ill-defined. Senescence occurs throughout life and can be beneficial in certain situations, such as tissue repair and homeostasis^{3,45}. Therefore, it is interesting to investigate whether certain manifestations of ciliopathies are caused by

dysregulated senescence. In order to achieve this, a thorough exploration of the cilia pathways and players involved in regulating senescence would not only aid in understanding the pathogenesis of ciliopathies but also has the potential to reveal new pharmaceutical pathways and candidates that could be targeted in diseases associated with senescence dysregulation.

Fig. 5 | The PML-NBs translocation of the CENEXIN1-FBF1 complex requires KIFC3 motor activity. **a** Diagram of WT and KIFC3 variants used in experiments. **b** Endogenous CENEXIN1 immunoprecipitates with V5-tagged WT or KIFC3^{DN} in RCTE cells, asterisk labels KIFC3^{DN}. **c** Immunofluorescent images showing localization of NeonGreen(NG)-tagged KIFC3 truncation variants (green) in RCTE cells. γ -tubulin (red) labels the ciliary base. Scale bar, 10 μ m. Immunofluorescence images showing the effect of re-expression of KIFC3 or KIFC3^{DN} on CENEXIN1 and FBF1 translocation. CENEXIN1 (green), FBF1 (red) and PML (cyan) were immunostained by antibodies, respectively (**d**) and quantitation of PML-NBs (**e**) in *shKIFC3* RCTE cells with or without IR exposure ($n = 40$ cells). Scale bar, 10 μ m. Immunofluorescence images showing the changes of CENEXIN1 (red) and PML (cyan) in control or over-expression NG-tagged KIFC3^{DN} RCTE cells with or without IR

treatment (**f**) and quantitation of PML-NBs numbers per cell ($n = 40$ cells) (**g**). Localization of KIFC3^{DN} was shown by NG direct fluorescence (green). Scale bar, 10 μ m. **h** SA- β -gal staining of IR-treated *shKIFC3* RCTE cells re-expressing KIFC3 or KIFC3^{DN}. Scale bar, 100 μ m. **i** Immunofluorescence images showing the impact on the PML-NBs translocation of CENEXIN1 (green) and FBF1 (red) after re-expressing CEP170C-tagged KIFC3 in IR-treated *shKIFC3* RCTE cells. γ -tubulin (cyan) labels the ciliary base. YFP direct fluorescence shown CEP170C-tagged KIFC3. Scale bar, 10 μ m. All results from $n = 3$ independent experiments. Data are the mean \pm SEM. Statistical significance was determined using one-way ANOVA. Three experiments were repeated independently with similar results (**b**, **c**, **h**, **i**). Source data are provided as a Source Data file.

Methods

Cell culture, treatments, and transfections

IMR90 (Cat# CCL-186), RCTE (Cat# CRL-4031), human embryonic kidney (HEK) 293 T cells (Cat# CRL-3216) were purchased from ATCC (American Type Culture Collection). IMR90 cells were cultured in ATCC-formulated Eagle's Minimum Essential Medium (30-2003) supplemented with penicillin/streptomycin (100 units/ml penicillin, 100 μ g/ml streptomycin; Life Technologies), and 10% fetal bovine serum (Thermo Fisher Scientific). Population doubling of less than 40 were used in the experiments. The RCTE cells were cultured in DMEM/F-12 containing 10% FBS. HEK293T cells were cultured in Dulbecco's modified Eagle's medium (DMEM) containing 10% FBS. Cellular senescence was induced in IMR90 and RCTE cells by exposing them to a relatively high dose of radiation for 10 Gy and 5 Gy, respectively. For IL1 β inducing senescence, RCTE cells were treated with IL-1 β (3 ng/ml) for 5 days. For Doxorubicin (DOX) inducing senescence, RCTE cells were treated with DOX (50 nM) for 48 h, then cultured in normal culture medium for 3 days. For colchicine treatment, IMR90 and RCTE cells were treated with colchicine 0.5 μ g/ml and 20 ng/ml, respectively, to induced MT disruption during senescence.

For plasmid transfection, X-tremeGENE 9 (Roche) was used following the manufacturer's manual. The siRNAs transfection experiment was performed by using lipofectamine RNAiMAX (Invitrogen) according to the manufacturer's protocol.

Stable cell lines

Establishment of stable cell lines were using lentivirus system. Briefly, co-transfected PCDH or pLKO.1 constructs with psPAX2 (Addgene #12260) and pMD2.G (Addgene #12259) into HEK293T cells to produce lentiviral particles that were collected 48 h after transfection for concentration by Lenti-X Concentrator (Takara) and the further infection of target cells. After overnight of lentivirus infection the cells were selected by G418 or puromycin for 3–7 days.

DNA constructs and siRNAs

Sub-cloning templates of human CENEXIN1 and KIFC3 were purchased from Addgene (#73334) and DNASU(#HsCD00442644), and ODF2(ISO6) was kindly provided by Dr. Kyung Lee (NIH/NCI). All full-length CDS of such gene with NG or v5 tag were inserted into PCDH vector. Construct of CENEXIN1 using for BioID analysis, we amplified and subcloned full-length CENEXIN1 into APEX2 tagged PCDH. The truncations of KIFC3 motor deficiency (C-terminal truncated aa 1-301) and Δ N cargo binding deletion (aa 304-687) were constructed by subcloning corresponding KIFC3 fragment into PCDH vector. For cilia limited KIFC3 expressing plasmid, full-length KIFC3 were inserted into N-terminal of YFP^{CEP170C} PCDH. Construct of KIFC3 and CENEXIN1 for BiFC assay, the cDNA of each gene was inserted into pBiFC-VN173 with FLAG tag (Addgene #22010) or pBiFC-VC155 with HA tag (Addgene #22011), respectively. Constructs of TLL5-EYFP, TLL6-EYFP, FBF1-myc same as described previously^{33,46}. Human KIFC2 was purchased from DNASU (#HsCD00877785). For construction of knockdown

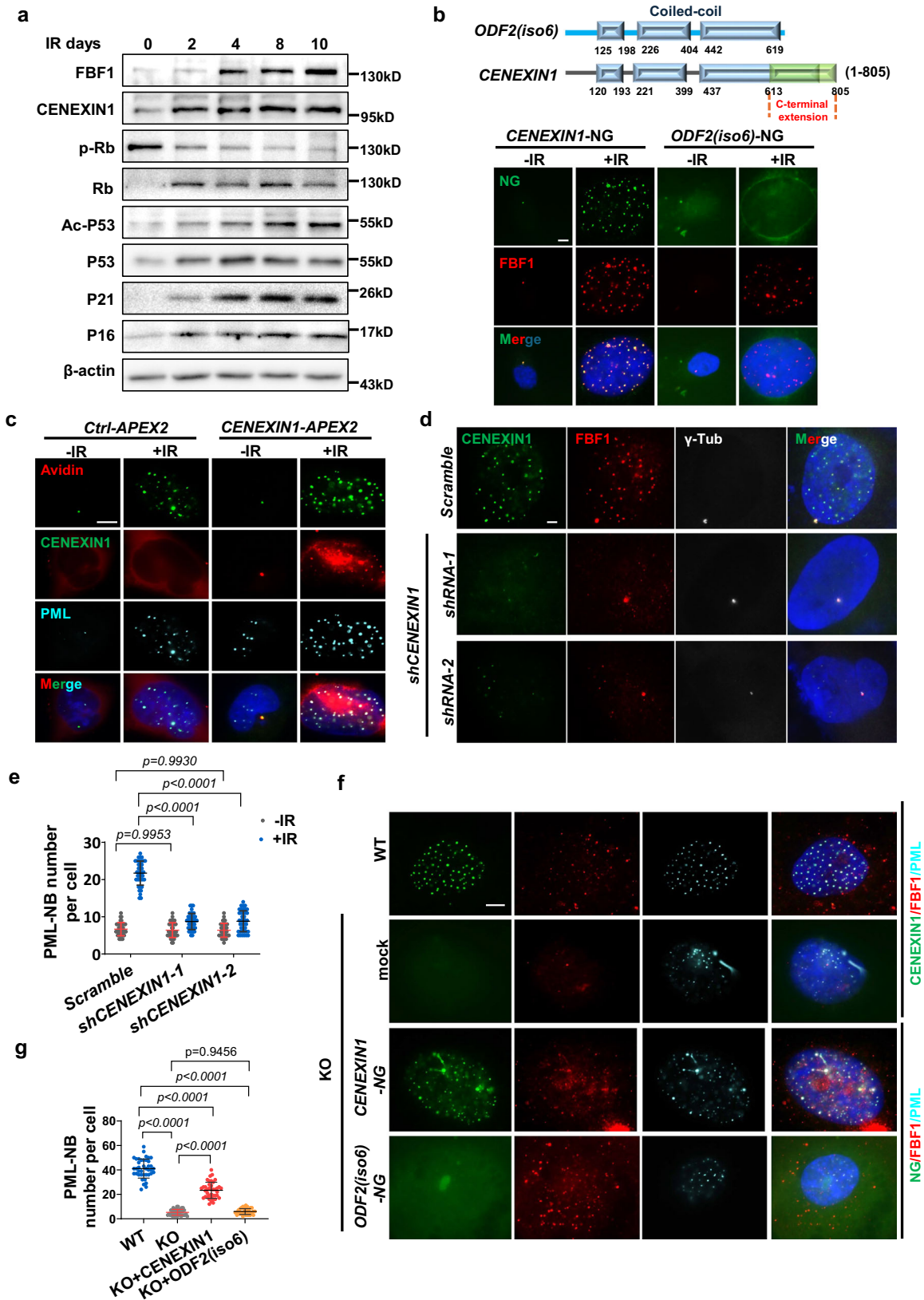
stable cell lines, shRNAs were inserted into pLKO.1-TRC plasmid following the Addgene instructions. Sequences of shRNA targeting corresponding mRNAs are as follows: *shCENEXIN1*#1: 5'-GCTTTATC-CACTCTGGAAT-3'; *shCENEXIN1*#2: 5'-GGCAGTTGGAGAGTGCCAT-3'; *shKIFC3*: 5'-GAAACATGTTGAGAAGGAA-3'; sequence of *shIFT88* were described previously⁴⁶. *shCDK5RAP2* were purchased from Sigma-Aldrich (TRC Clone ID #TRCN0000128328, TRCN0000323174); *shTLL5* were purchased from Sigma-Aldrich (TRC Clone ID # TRCN0000153923, TRCN0000338450); *shTLL6* were purchased from Sigma-Aldrich (TRC Clone ID # TRCN0000127680, TRCN0000127969); *shFBF1* were purchased from Sigma-Aldrich (TRC Clone ID # TRCN0000253800). The siRNA duplexes of *siCDK5RAP2* and negative control were purchased from Invitrogen (#s31429, #12935300), *siDYNC1LI1* were purchased from Invitrogen (#118332). Sequences of *siCenexin1* were same as using in shRNA synthesis, and *siFBF1*, *siTLL5*, *siTLL6* same as described previously^{33,36,47}.

Western blotting

Cells were washed with phosphate-buffered saline (PBS) for three times and homogenized in RIPA buffer (Boston Bioproducts, #BP-115D) with protease inhibitors (Roche) on ice for 15 min and centrifuged at 13,000 g for 20 min at 4 $^{\circ}$ C. Supernatant containing protein were collected and measured concentration by BCA method (ThermoFisher). 15 μ g of protein were loaded on SDS-PAGE gels and transferred to polyvinylidene fluoride membranes (Millipore). The membranes were blocked with 5% non-fat milk for 1 h, and then incubated with primary and secondary antibodies. Chemical luminescence (BIO-RAD) was used to develop signal and images were obtained using ChemiDoc Touch Imaging System (BIO-RAD).

Antibodies

Primary antibodies: α -tubulin (HPA043684; dilution 1:500 for immunofluorescent), CENEXIN1 (HPA001874; 1:500 for western blotting) from Atlas antibodies; EB1 (sc-47704; dilution 1:500 for immunofluorescent), PML (PG-M3) (sc-966; dilution 1:1000 for immunofluorescent), HYL51 (D-9) (sc-376721; dilution 1:200 for immunofluorescent), p21 (sc-6246; dilution 1:500 for western blotting), GFP tag (sc9996; dilution 1:1000 for western blotting), CDK5RAP2 (sc-517321; dilution 1:1000 for western blotting) from Santa Cruz; ac-p53 (2525; dilution 1:1000 for western blotting), Phospho-Rb (Ser807/S811) (8516; dilution 1:1000 for western blotting), Rb (9313; dilution 1:1000 for western blotting), p53 (2527; dilution 1:1000 for western blotting) from Cell Signaling technology; ciliary base marker CENTRIN2 (20H5, a generous gift from Jeffrey Salisbury; dilution 1:250 for immunofluorescent), FBF1 (11531-1-AP; dilution 1:500 for immunofluorescent and 1:1000 for western blotting), p16INK4a (10883-1-AP; dilution 1:1000 for western blotting), KIFC3 (10125-2-AP; dilution 1:1000 for immunofluorescent and western blotting), CAMSAP2 (17880-1-AP; dilution 1:500 for immunofluorescent), HA tag (51064-2-AP; dilution 1:1000 for immunofluorescent) from Proteintech; glutamylated tubulin (GT335) (AG-20B-0020-C100; dilution 1:500 for immunofluorescent and 1:1000 for western blotting) from AdipoGen



Life Science; v5 tag (MA5-15253; dilution 1:1000 for immunofluorescent, 1:1000 for western blotting, and 1 μg for immunoprecipitation), α-tubulin (A11126; dilution 1:100 for immunofluorescent), NESPRIN-1 (PA5-115640; dilution 1:500 for immunofluorescent), ARL13B (66739-1-IG; dilution 1:500 for immunofluorescent), CDK5RAP2 (702394; dilution 1:500 for immunofluorescent) from

Invitrogen; acetylated tubulin (T7451, dilution 1:5000 for immunofluorescent), β-actin (A1978; dilution 1:2000 for western blotting), γ-tubulin (T5326; dilution 1:1000 for immunofluorescent), Myc tag (SAB2702192; dilution 1:2000 for western blotting), FLAG tag (F1804; dilution 1:1000 for immunofluorescent) from Sigma; CENEXIN1 (H00004957-M01; dilution 1:500 for immunofluorescent) from

Fig. 6 | CENEXINI but not the shorter ODF2(iso6) isoform regulates the PML-NBs translocation of FBF1. **a** Western blot showing changes of CENEXINI, FBF1, and senescence markers in IR-treated RCTE cells. **b** Immunofluorescence images of RCTE cells expressing NG tagged-CENEXINI or short isoform ODF2 (iso6) with or without IR treatment. FBF1 (red) was immunostained by antibody. CENEXINI or ODF2 (iso6) was shown by NG direct fluorescence (green). Scale bar, 10 μ m. **c** Nuclear PML-NBs translocation of CENEXINI and biotinylated proteins in control or APEX2-tagged CENEXINI over-expression RCTE cells with or without IR treatment. Endogenous CENEXINI (green) and PML (cyan) were labeled with antibody, respectively. Biotinylated proteins were labeled with streptavidin (red). Scale bar, 10 μ m. Immunofluorescence images showing nuclear translocation of FBF1 (**d**) and

quantitation of PML-NBs number (**e**) in IR-treated control or *shCENEXINI* RCTE cells ($n = 40$ cells). γ -tubulin (white) labels ciliary base. Scale bar, 10 μ m. Immunofluorescence images showing the rescuing effect of re-expressing NG-tagged CENEXINI or ODF2 (iso6) (**f**) and quantitation of PML-NBs number (**g**) in IR-treated control or *CENEXINI*^{-/-} RCTE cells ($n = 40$ cells). CENEXINI or ODF2 (iso6) was shown by NG direct fluorescence. Endogenous CENEXINI (green), FBF1 (red) and PML (cyan) were labeled with antibody, respectively. Scale bar, 10 μ m. All results from $n = 3$ independent experiments. Data are the mean \pm SEM. Statistical significance was determined using one-way ANOVA. Three experiments were repeated independently with similar results (**a-c**). Source data are provided as a Source Data file.

Abnova; NUP153 (ab84872; dilution 1:1000 for immunofluorescent.) from Abcam. Secondary antibodies: Peroxidase-AffiniPure Goat anti-mouse (111-035-144) or anti-rabbit (115-035-146) from Jackson ImmunoResearch Laboratories, dilution 1:2000 for western blotting. Goat anti-Rabbit IgG (H + L) Highly Cross-Adsorbed Secondary Antibody, Alexa Fluor 488 (A-11034) or 555 (A-21429), Goat anti-Mouse IgG1 Cross-Adsorbed Secondary Antibody, Alexa Fluor 555 (A-21127) or 488 (A-21121) or 647 (A-21240), Goat anti-Mouse IgG2a Cross-Adsorbed Secondary Antibody, Alexa Fluor 488 (A-21131) or 555 (A-21137) or 647 (A-21241), Goat anti-Mouse IgG2b Cross-Adsorbed Secondary Antibody, Alexa Fluor 647 (A-21242) from Invitrogen, dilution 1:1000 for immunofluorescent.

Bio-ID

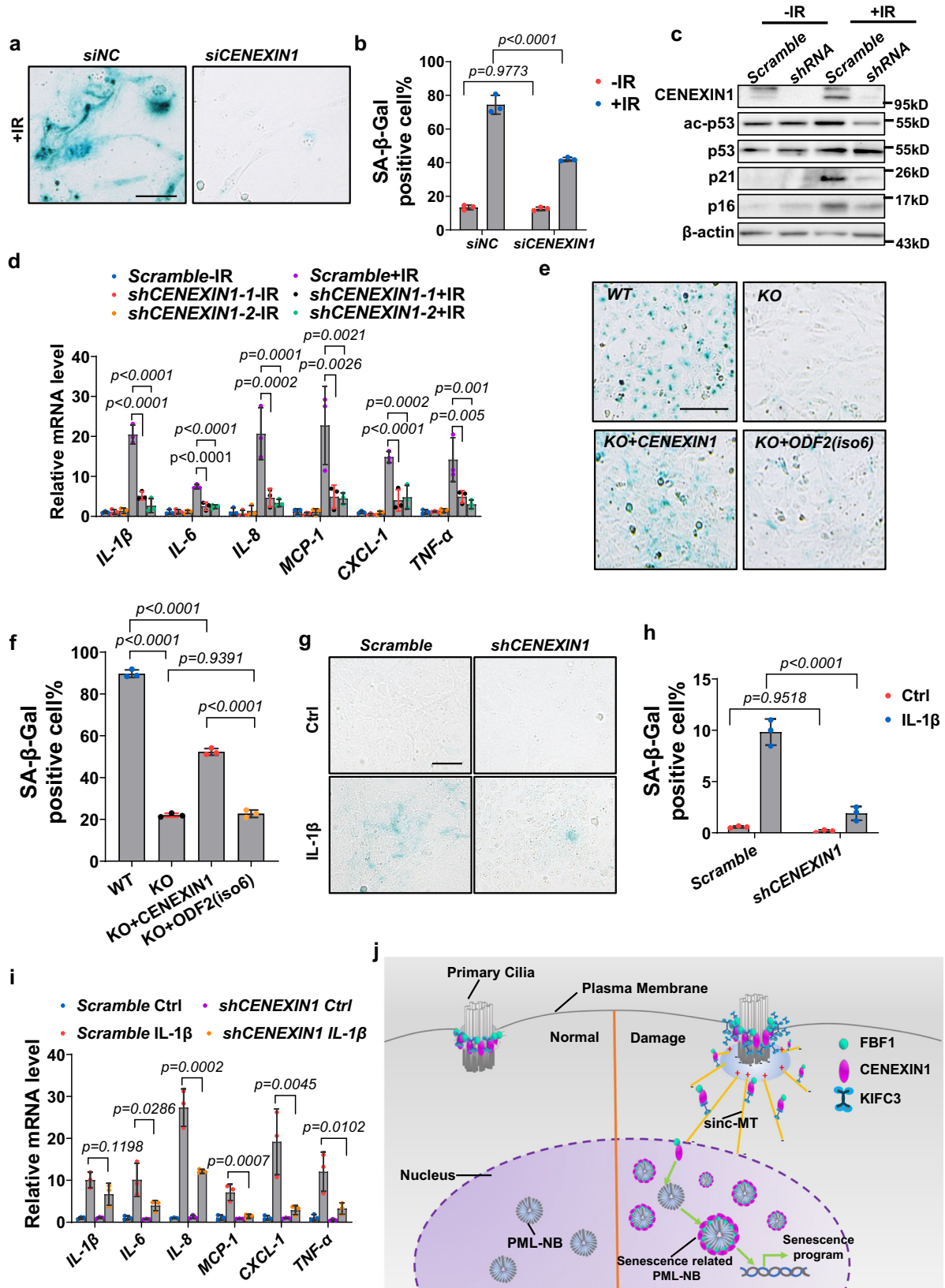
For FBF1 BioID, RCTE cells expressing either BirA alone or FBF1-BirA were cultured until reaching approximately 50% confluence and then exposed to 5 Gy of ionizing radiation (IR). Samples were collected at day 0 (without IR) and day 10 after IR exposure. The total number of samples analyzed $n = 4$. The cells expressing BirA alone in each condition were used as control. In the day 0 sample (without IR), the same cells were taken to the IR room but not exposed to IR. Cells ($\sim 4 \times 10^7$) were incubated for 24 h in complete media supplemented with 1 μ g/ml doxycycline and 50 μ M biotin. After three PBS washes, cells were lysed at 25 $^{\circ}$ C in 1 ml lysis buffer (50 mM Tris, pH 7.4, 500 mM NaCl, 0.4% SDS, 5 mM EDTA, 1 mM DTT, and 1x Complete protease inhibitor) and sonicated, followed by centrifugation at 15,000 \times g. Supernatants were incubated with 600 μ l Dynabeads overnight. After washing with wash buffers, bound proteins were removed from the magnetic beads with 50 μ l of SDS-sample buffer saturated with biotin at 98 $^{\circ}$ C. Ten percent of the sample was used for Western blotting, while 90% of the sample was analyzed by mass spectrometry (MS). Proteins eluted from the streptavidin beads using SDS-sample buffer were alkylated and separated by 1D SDS-PAGE, followed by Coomassie blue staining. The entire gel lane was cut, destained, and subjected to in-gel digestion for subsequent MS analysis.

For CENEXINI(ODF2) APEX2 based BioID, RCTE cells expressed either APEX2 or CENEXINI-APEX2 were cultured to approximately 80% confluency and incubated with 500 μ M biotin-phenol (BP) for 30 min at 37 $^{\circ}$ C, then add H₂O₂ to achieve the final concentration of 1 mM to incubate the cells for 1 min at room temperature. Quickly aspirate labeling and quenched the cells with wash buffer. The cells were lysate in RIPA buffer containing protease inhibitors on ice for 20 min followed by 15,000 \times g 20 min centrifugation at 4 $^{\circ}$ C. Supernatant were collected for the further analysis. After measured concentration for each sample, 10–12 mg protein lysate rotated with 200 μ l of streptavidin beads overnight at 4 $^{\circ}$ C. The biotinylated proteins captured by streptavidin were followed by on-beads digestion and MS analysis. Negative controls that omit APEX2, BP or H₂O₂ were included and detected by western blot to assess nonspecific or endogenous peroxidase activity. CENEXINI translocation was detected by immunofluorescence using Streptavidin Alexa Fluor 555 Conjugate (s32355) from Invitrogen, dilution 1:1000. The captured the biotinylated proteins were washed to remove unbound protein then solubilized in 8 M

urea/50 mM TEAB pH 8.0 for reduction with TCEP and alkylation with iodoacetamide. The solution was diluted with 50 mM Tris pH 8.0 and trypsin added for overnight digestion at 37 $^{\circ}$ C. The extracted peptides were acidified and desalted using a C18 spin column and concentrated on a SpeedVac spinning concentrator. Both projects were analyzed using one biological replicate.

The peptide mixture was solubilized in 0.2% trifluoroacetic acid for analysis by nano-flow liquid chromatography electrospray tandem mass spectrometry (nanoLC-ESI-MS/MS) using a ThermoFinnigan QExactive Mass Spectrometer (Thermo Fisher Scientific, Bremen, Germany) coupled to Thermo Ultimate 3000 RSLCnano HPLC system. The samples were loaded onto a 250 nl OPTI-PAK trap (Optimize Technologies, Oregon City, OR) custom packed with Halo 2.7 μ m C18 solid phase and chromatography was performed using 0.2% formic acid in both the A solvent (98%water/2%acetonitrile) and B solvent (80% acetonitrile/10% isopropanol/10% water), running a 5%B to 40%B gradient over 60 min at 400 nl/min through a hand packed PicoFrit (New Objective, Woburn, MA) 100 μ m \times 350 mm column (Agilent PoroShell EC-C18, 2.7 μ m). The Q-Exactive mass spectrometer experiment was a data dependent set up with a MS1 survey scan from 340 to 1500 m/z at resolution 70,000 (at 200 m/z), followed by HCD MS/MS scans on the top 15 ions having a charge state of +2, +3, or +4, at resolution 17,500 and with the NCE set to 26. The ions selected for MS/MS were placed on an exclusion list for 30 s. The MS1 AGC target were set to 1e6 and the MS2 target was set to 1e5 with max ion inject times of 50 ms for both.

Tandem mass spectra were extracted by msconvert version 3.0.9134. Charge state deconvolution and deisotoping was not performed. All MS/MS samples were analyzed using Mascot (Matrix Science, London, UK; version 2.4.0) and X! Tandem (The GPM, thegpm.org; version X! Tandem Sledgehammer (2013.09.01.1)). Mascot and X! Tandem was set up to search a current Swissprot database with reverse decoy (# entries) assuming the digestion enzyme stricttrypsin and with a fragment ion mass tolerance of 0.020 Da and a parent ion tolerance of 10.0 PPM. Glu->pyro-Glu of the n-terminus, ammonia-loss of the n-terminus, gln->pyro-Glu of the n-terminus, and oxidation of methionine were specified in X! Tandem as variable modifications and carbamidomethyl of cysteine was specified as a fixed modification. Oxidation of methionine and carbamidomethyl of cysteine were specified in Mascot as variable modifications and fixed modifications respectively. Scaffold (version Scaffold_4.8.3, Proteome Software Inc., Portland, OR) was used to validate MS/MS based peptide and protein identifications. Peptide identifications were accepted if they could be established at greater than 95.0% probability by the Scaffold Local FDR algorithm. Protein identifications were accepted if they could be established at greater than 95.0% probability and contained at least 2 identified peptides. Protein probabilities were assigned by the Protein Prophet algorithm. Proteins that contained similar peptides and could not be differentiated based on MS/MS analysis alone were grouped to satisfy the principles of parsimony. Proteins sharing significant peptide evidence were grouped into clusters. Protein comparisons are made with ratios of Scaffold normalized total spectral counts. The mass spectrometry proteomics data have been deposited to the



ProteomeXchange Consortium via the PRIDE⁴⁸ partner repository with the dataset identifier PXD045355 and 10.6019/PXD045355.

Immunofluorescence microscopy and SIM

Cells were fixed with methanol for 20 min at -20°C followed by PBS wash for three times, and then blocked with 3% BSA overnight at 4°C .

Cells were sequentially incubated with primary and secondary antibodies. To stain microtubules using the α -tubulin antibody, we used an enhanced immunofluorescence. Cells were prefixed with 0.4% paraformaldehyde for 5 min at 37°C , extracted with 0.5% Triton X-100 in PHEM (50 mM PIPES, 50 mM HEPES, 10 mM EGTA and 10 mM MgCl_2 , pH 6.9) for 2 min at 37°C and then stained following the

Fig. 7 | CENEXIN1 deficiency suppresses senescence induction. **a–d** SA- β -gal staining (**a**), quantitation of SA- β -gal-positive cells ($n = 3$ independent experiments, 6–8 fields per experiment, 200 cells per field) (**b**) in control or *shCENEXIN1* RCTE cells with or without IR exposure. Western blot of senescence markers (**c**), and relative mRNA level of SASP genes (**d**) in control or *shCENEXIN1* RCTE cells with or without IR exposure. For IR treatment, cells were collected at day 10 after irradiation. Scale bar, 100 μ m. SA- β -gal staining (**e**) and quantitation of SA- β -gal-positive cells ($n = 3$ independent experiments, 6–8 fields per experiment, 200–300 cells per field) (**f**), in control or *CENEXIN1*^{+/−}RCTE cells re-expressing CENEXIN1 or ODF2 (iso6) at day 10 after IR exposure. Scale bar, 100 μ m. SA- β -gal staining (**g**), quantitation of SA- β -gal-positive cells ($n = 3$ independent experiments, 3–4 fields per experiment, 200–500 cells per field) (**h**), and relative mRNA level of SASP genes (**i**) in IL-1 β -treated

(3 ng/ml for 5 days) control or *shCENEXIN1* RCTE cells. Scale bar, 50 μ m. **j** Proposed working model: Exposure to irreparable stresses triggers the reorganization of microtubules (MTs), leading to the nucleation of sinc-MTs in the proximity of the nuclear envelop towards the ciliary base. Concurrently, the minus-end-directed kinesin KIFC3 is recruited to the ciliary base. It subsequently facilitates the transportation of the CENEXIN1-FBF1 cargo complex along the sinc-MTs, directing it towards the nucleus. This process initiates cellular senescence in stressed human cells. All results from $n = 3$ independent experiments. Data are the mean \pm SEM. Statistical significance was determined using one-way ANOVA. Three experiments were repeated independently with similar results (**c**). Source data are provided as a Source Data file.

immunofluorescence procedure described above. Fluorescence images were acquired using Nikon TE2000-U with Metamorph software (Molecular Devices). Images were captured using Ti Microscope equipped with Plan Apo VC 60X Oil DIC N2 objective lens, calibration (μ m/px) 0.11, widefield image captured filter with GFP, TxRed, CY5, DAPI. Three-dimensional structured illumination microscopy (3D-SIM) analysis were performed by using a Zeiss ELYRA super-resolution microscopy system equipped with an alpha 'Plan-Apochromat' 100x/1.46 Oil DIC oil immersion objective and an Andor iXon 885 EMCCD camera following the standard protocols. Structured illumination reconstruction and image processing were performed using ZEN software package (Zeiss) followed by 3D rendering analysis using Imaris 8 software (Oxford Instruments). Confocal Images, Z-stacks, and Tilesans were obtained using a ZEISS LSM980 series inverted confocal microscope with AiryScan 2 super-resolution capabilities. Images were captured using Plan-Apochromat 63X/1.40 Oil DIC M27 objective lens, laser emission wavelength with 568 nm, 517 nm, 465 nm, pixel time 1.37 μ s, frame time 7.55 s, LSM Scan Speed 6 Bidirectional scan. ZEN Blue, the accompanying software to the LSM980 confocal series, was used to acquire, process, and export the resulting data. Huygens Essential 23.10 was used to process image deconvolution.

Live cell imaging

StayGold-KIFC3 or EB1-GFP (Addgene #17234) expressing RCTE stable cells were cultured in petridish (ThermoFisher Scientific Inc.) At 24 h after plating cells at 40–50% confluence in DMEM/F12 medium, cellular senescence was induced by exposing cells to 5 Gy radiation. 24 h after IR treatment, the cells were placed in live-cell imaging culture chambers (Tokai Hit microscope stage top incubator) that set on Nikon ECLIPSE Ti microscope. Images were captured using Ti Microscope equipped with Plan Apo VC 60X Oil DIC N2 objective lens, calibration (μ m/px) 0.11, widefield image captured filter with GFP, DAPI, at 1 s interval.

Immunoprecipitation assay

For Co-IP experiment, the tagged plasmids of were co-transfected into HEK293T cells for 48–72 h. Cells were lysed in ice-cold IP buffer (25 mM Tris-HCl, pH 7.4, 150 mM NaCl, 0.5% NP-40, 1 mM EDTA) with protease inhibitor cocktail (Roche). The lysate was cleaned by centrifugation for 20 min with 12,000 *g* at 4 °C, then the supernatant was collected for pre-cleared using protein-G beads for 4 h at 4 °C. The pre-cleared supernatant was then incubated with protein-G beads with primary antibodies or control IgG overnight at 4 °C. After washing with IP buffer for three times, the beads bound immune complex were eluted using 1 \times SDS loading buffer and detected by western blotting. To perform Co-IP experiments with endogenous proteins during senescence, stable RCTE cell line expressed tagged protein of interest were exposed 5 Gy of radiation. After lysing and pre-clearing, the supernatant was incubated with protein-G beads and appropriate primary antibodies of endogenous protein or tagged protein following

conventional protocol described above. The immunocomplexes were separated by SDS-PAGE gels and analyzed.

CRISPR-Cas9 gene editing

CENEXIN1 guide RNA (gRNA) was designed using an online tool (<https://zlab.bio/guide-design-resources>) and subcloned into pSpCas9(BB)–2A-GFP (px458) vector which was then transfected into RCTE cells for 48 h. Then flow cytometry sorting was performed to select GFP-positive cells into 96 well plate for single clone expansion. gRNA sequence was as follows: GUGAUCUCCAGGCAAUGAGG. Further knockout efficiency was confirmed by immunofluorescence analysis and western blotting.

Real-time RT-PCR

Total RNA was extracted from cells using TRIzol reagent (Invitrogen #15596-026). mRNAs were reverse transcribed into cDNAs by using the High-Capacity cDNA Reverse Transcription Kit (Applied Biosystems #00351115). Real-time PCR was performed using SYBR Green PCR Master Mix (GeneCopoeia #HmiRQP2641) with specific primers of each candidate gene and detected by CFX384 Real-Time system (Bio-Rad). Relative expression levels were shown as 2^{−ΔΔCt} and glyceraldehyde-3-phosphate dehydrogenase (GAPDH) as reference gene. PCR primers used are listed in Table S3 in Supplementary Data.

SA- β -gal staining

Senescence Associated (SA)-beta-gal staining was performed according to the manufacturer's instructions (Cell signaling). Cells were fixed with 1 \times Fixative solution for 10 min at room temperature. After washing with 1 \times PBS for twice, the cells were incubated with β -Galactosidase Staining Solution of pH 6.0 in a sealed plate overnight at 37 °C. The ratio of SA- β -gal positive/total cells were used as percentage of SA- β -gal-positive. 6–8 fields with \geq 100 cells per field were examined.

TUNEL assay

Apoptosis was detected with a TUNEL assay kit (DeadEnd™ Fluorometric TUNEL System, G3250, Promega) following the manufacturer's protocol.

Bimolecular Fluorescence Complementation (BiFC) Assay

RCTE cells reached ~70% confluence were transfected with BiFC constructs (N-terminal domain of the Venus fluorescent tagged (VN) KIFC3 (VN-KIFC3) with an additional FLAG tag and the C-terminal domain of the Venus fluorescent tagged (VC) CENEXIN1 (VC-CENEXIN1) with an additional HA tag) using the TRANSIT-X2 reagent (Mirus Bio) according to the manufacturer's instructions. After 24 h of transfection, cells were exposed to 5 Gy of IR. Cells were collected at specific time point and washed with PBS and fixed with methanol for 20 min at −20 °C followed by PBS wash for three times, and then blocked with 3% BSA overnight at 4 °C. Fixed cells were incubated with FLAG tag and HA tag primary antibody and Goat anti-Mouse IgG1 Alexa Fluor 647 and Goat anti-Rabbit IgG (H+L) Alexa Fluor 555 secondary antibody

sequentially. Venus protein reconstituted fluorescence were visualized using Nikon Ti Microscope equipped with Plan Apo VC 60X Oil DIC N2 objective lens, widefield image captured filter with GFP. FLAG tagged KIFC3 and HA tagged CENEXIN1 immunofluorescence captured by using TxRed and CY5 filter.

Statistical analysis

The statistical analyses were performed with GraphPad Prism 9.3.1. No statistical method was used to predetermine sample size. Sample size was determined to be adequate based on the magnitude and consistency of measurable differences between groups. It was also chosen on the basis of prior studies that showed significant effects with similar sample sizes. Three biological replicates were used in each experiment unless otherwise stated. Samples were randomly allocated to experimental and control groups. Data are presented as mean \pm SEM. Statistical significance was calculated by Two-tailed Unpaired Student's *t* test and one-way ANOVA followed by multiple comparisons. $P < 0.05$ were considered as statistically significant difference. The exact *P* values were added in the figure. No data were excluded from the analyses. Data collection was performed while blinded, utilizing random numbers for labeling.

Reporting summary

Further information on research design is available in the Nature Portfolio Reporting Summary linked to this article.

Data availability

The proteomics data generated in this study have been deposited in the PRIDE database under accession code PXD045355 [<http://www.ebi.ac.uk/pride/archive/projects/PXD045355>]. All data supporting the findings of this study are available in main manuscript and Supplementary Information. Additional data associated with the paper and source data file are shared on Figshare [<https://doi.org/10.6084/m9.figshare.26831683>]. Source data are provided with this paper.

References

- Kirkland, J. L. & Tchonia, T. Cellular senescence: a translational perspective. *EBioMedicine* **21**, 21–28 (2017).
- Campisi, J. & d'Adda di Fagagna, F. Cellular senescence: when bad things happen to good cells. *Nat. Rev. Mol. Cell Biol.* **8**, 729–740 (2007).
- Faget, D. V., Ren, Q. & Stewart, S. A. Unmasking senescence: context-dependent effects of SASP in cancer. *Nat. Rev. Cancer* **19**, 439–453 (2019).
- Xu, M. et al. Targeting senescent cells enhances adipogenesis and metabolic function in old age. *Elife* **4**, e12997 (2015).
- Baker, D. J. et al. Clearance of p16Ink4a-positive senescent cells delays ageing-associated disorders. *Nature* **479**, 232–236 (2011).
- Xu, M. et al. Senolytics improve physical function and increase lifespan in old age. *Nat. Med.* **24**, 1246–1256 (2018).
- Zhang, X. et al. Characterization of cellular senescence in aging skeletal muscle. *Nat. Aging* **2**, 601–615 (2022).
- Singla, V. & Reiter, J. F. The primary cilium as the cell's antenna: signaling at a sensory organelle. *Science* **313**, 629–633 (2006).
- Goetz, S. C. & Anderson, K. V. The primary cilium: a signalling centre during vertebrate development. *Nat. Rev. Genet.* **11**, 331–344 (2010).
- Badano, J. L., Mitsuma, N., Beales, P. L. & Katsanis, N. The ciliopathies: an emerging class of human genetic disorders. *Annu. Rev. Genom. Hum. Genet.* **7**, 125–148 (2006).
- Adams, M., Smith, U. M., Logan, C. V. & Johnson, C. A. Recent advances in the molecular pathology, cell biology and genetics of ciliopathies. *J. Med. Genet.* **45**, 257–267 (2008).
- Ma, X. et al. A stress-induced cilium-to-PML-NB route drives senescence initiation. *Nat. Commun.* **14**, 1840 (2023).
- Salomoni, P. & Pandolfi, P. P. The role of PML in tumor suppression. *Cell* **108**, 165–170 (2002).
- Ferbeyre, G. et al. PML is induced by oncogenic ras and promotes premature senescence. *Genes Dev.* **14**, 2015–2027 (2000).
- Voter, W. A. & Erickson, H. P. The kinetics of microtubule assembly. Evidence for a two-stage nucleation mechanism. *J. Biol. Chem.* **259**, 10430–10438 (1984).
- Sanchez, A. D. & Feldman, J. L. Microtubule-organizing centers: from the centrosome to non-centrosomal sites. *Curr. Opin. Cell Biol.* **44**, 93–101 (2017).
- Hirokawa, N. Kinesin and dynein superfamily proteins and the mechanism of organelle transport. *Science* **279**, 519–526 (1998).
- Westermann, S. & Weber, K. Post-translational modifications regulate microtubule function. *Nat. Rev. Mol. Cell Biol.* **4**, 938–947 (2003).
- Wloga, D., Joachimiak, E. & Fabczak, H. Tubulin post-translational modifications and microtubule dynamics. *Int. J. Mol. Sci.* **18**, <https://doi.org/10.3390/ijms18102207> (2017).
- Janke, C. & Magiera, M. M. The tubulin code and its role in controlling microtubule properties and functions. *Nat. Rev. Mol. Cell Biol.* **21**, 307–326 (2020).
- Moujaber, O. et al. Cellular senescence is associated with reorganization of the microtubule cytoskeleton. *Cell Mol. Life Sci.* **76**, 1169–1183 (2019).
- Huber, D., Geisler, S., Monecke, S. & Hoyer-Fender, S. Molecular dissection of ODF2/Cenexin revealed a short stretch of amino acids necessary for targeting to the centrosome and the primary cilium. *Eur. J. Cell Biol.* **87**, 137–146 (2008).
- Tateishi, K. et al. Two appendages homologous between basal bodies and centrioles are formed using distinct Odf2 domains. *J. Cell Biol.* **203**, 417–425 (2013).
- Chang, J. et al. Essential role of Cenexin1, but not Odf2, in ciliogenesis. *Cell Cycle* **12**, 655–662 (2013).
- Meqbel, B. R. M., Gomes, M., Omer, A., Gallouzi, I. E. & Horn, H. F. LINCing senescence and nuclear envelope changes. *Cells* **11**, <https://doi.org/10.3390/cells11111787> (2022).
- Vitre, B. et al. EB1 regulates microtubule dynamics and tubulin sheet closure in vitro. *Nat. Cell Biol.* **10**, 415–421 (2008).
- Akhmanova, A. & Steinmetz, M. O. Control of microtubule organization and dynamics: two ends in the limelight. *Nat. Rev. Mol. Cell Biol.* **16**, 711–726 (2015).
- Jiang, K. et al. Microtubule minus-end stabilization by polymerization-driven CAMSAP deposition. *Dev. Cell* **28**, 295–309 (2014).
- Choi, Y. K., Liu, P., Sze, S. K., Dai, C. & Qi, R. Z. CDK5RAP2 stimulates microtubule nucleation by the gamma-tubulin ring complex. *J. Cell Biol.* **191**, 1089–1095 (2010).
- Edde, B. et al. Posttranslational glutamylation of alpha-tubulin. *Science* **247**, 83–85 (1990).
- Gaertig, J. & Wloga, D. Ciliary tubulin and its post-translational modifications. *Curr. Top. Dev. Biol.* **85**, 83–113 (2008).
- Audebert, S. et al. Developmental regulation of polyglutamylated alpha- and beta-tubulin in mouse brain neurons. *J. Cell Sci.* **107**, 2313–2322 (1994).
- He, K. et al. Axoneme polyglutamylation regulated by Joubert syndrome protein ARL13B controls ciliary targeting of signaling molecules. *Nat. Commun.* **9**, 3310 (2018).
- Ebberink, E. et al. Tubulin engineering by semi-synthesis reveals that polyglutamylation directs detyrosination. *Nat. Chem.* **15**, 1179–1187 (2023).
- Ambrose, J. C., Li, W., Marcus, A., Ma, H. & Cyr, R. A minus-end-directed kinesin with plus-end tracking protein activity is involved in spindle morphogenesis. *Mol. Biol. Cell* **16**, 1584–1592 (2005).
- Zhang, Y. et al. BFB1 deficiency promotes beigeing and healthy expansion of white adipose tissue. *Cell Rep.* **36**, 109481 (2021).

37. Hung, V. et al. Spatially resolved proteomic mapping in living cells with the engineered peroxidase APEX2. *Nat. Protoc.* **11**, 456–475 (2016).
38. Slaats, G. G. et al. Nephronophthisis-associated CEP164 regulates cell cycle progression, apoptosis and epithelial-to-mesenchymal transition. *PLoS Genet.* **10**, e1004594 (2014).
39. Chaki, M. et al. Exome capture reveals ZNF423 and CEP164 mutations, linking renal ciliopathies to DNA damage response signaling. *Cell* **150**, 533–548 (2012).
40. van Dijk, J. et al. A targeted multienzyme mechanism for selective microtubule polyglutamylation. *Mol. Cell* **26**, 437–448 (2007).
41. Janke, C. et al. Tubulin polyglutamylase enzymes are members of the TTL domain protein family. *Science* **308**, 1758–1762 (2005).
42. Rogowski, K. et al. A family of protein-deglutamylating enzymes associated with neurodegeneration. *Cell* **143**, 564–578 (2010).
43. Hata, S. et al. The balance between KIFC3 and EG5 tetrameric kinesins controls the onset of mitotic spindle assembly. *Nat. Cell Biol.* **21**, 1138–1151 (2019).
44. Mylonas, K. J. et al. Cellular senescence inhibits renal regeneration after injury in mice, with senolytic treatment promoting repair. *Sci. Transl. Med.* **13**, <https://doi.org/10.1126/scitranslmed.abb0203> (2021).
45. He, S. & Sharpless, N. E. Senescence in Health and Disease. *Cell* **169**, 1000–1011 (2017).
46. Xiaoyu Ma, Y. Z. et al. A stress-induced cilium-to-PML-NB route drives senescence initiation. *Nat. Commun.* **14**, 1840 (2022).
47. Wei, Q. et al. Transition fibre protein FBF1 is required for the ciliary entry of assembled intraflagellar transport complexes. *Nat. Commun.* **4**, 2750 (2013).
48. Perez-Riverol, Y. et al. The PRIDE database resources in 2022: a hub for mass spectrometry-based proteomics evidences. *Nucleic Acids Res.* **50**, D543–D552 (2022).

Acknowledgements

We thank Dr. Takanari Inoue (Johns Hopkins University School of Medicine) for sharing cilia trapping system and Dr. Kyung S. Lee (NIH/NCI) for sharing ODF2 plasmid. We thank Mayo Proteomic Core for BioID analysis which is a shared resource of the Mayo Clinic Cancer Center (NCI P30 CA15083). We thank Mayo Microscopy and Cell Analysis Core for Confocal and SIM image. This work was supported from the National Institutes of Health (NIH) research grants R01DK090038, R01DK099160, R01AG076469, the Mayo Clinic Robert M. and Billie Kelley Pirnie Translational Polycystic Kidney Disease Center, the Mayo Robert and Arlene Kogod Center on Aging, and Mayo Clinic Foundation to J.H.; the American Society of Nephrology Foundation KidneyCure Donald E. Wesson Research Fellowship Award to J.H.R.; the Department of Defense (W81XWH2010214 and HT94252410154), NIDDK R01DK139607, Pilot and Feasibility subawards from Mayo Clinic Translational PKD Center (P30DK90728), and Baltimore PKD Center (2P30DK090868) to K.L.

Author contributions

J.H. generated the hypothesis and J.H. and K.L. designed the experiments. J.H.R., Y.Z., and C.C. conducted most experiments. K.H. established stable cell line, constructs of TTL5/6-EYFP, CEP170C-PCDH vector, NG-PCDH vector, and siRNA for TTL5/6. J.H.R. and Y.Z. contributed to the immunofluorescence experiments. J.H.R. and C.C. contributed to proteomics. J.H.R., C.C., K.H., and X.S. contributed to the plasmid design and construction. Y.H., X.Z., X.M., G.H., C.G.M., Z.D., and N.K.L. contributed reagents, proteomics analysis, and discussed data. J.H.R. and J.H. wrote the manuscript with input from all coauthors.

Competing interests

The authors declare no competing interests.

Additional information

Supplementary information The online version contains supplementary material available at <https://doi.org/10.1038/s41467-024-52363-w>.

Correspondence and requests for materials should be addressed to Jinghua Hu.

Peer review information *Nature Communications* thanks the anonymous reviewers for their contribution to the peer review of this work. A peer review file is available.

Reprints and permissions information is available at <http://www.nature.com/reprints>

Publisher's note Springer Nature remains neutral with regard to jurisdictional claims in published maps and institutional affiliations.

Open Access This article is licensed under a Creative Commons Attribution-NonCommercial-NoDerivatives 4.0 International License, which permits any non-commercial use, sharing, distribution and reproduction in any medium or format, as long as you give appropriate credit to the original author(s) and the source, provide a link to the Creative Commons licence, and indicate if you modified the licensed material. You do not have permission under this licence to share adapted material derived from this article or parts of it. The images or other third party material in this article are included in the article's Creative Commons licence, unless indicated otherwise in a credit line to the material. If material is not included in the article's Creative Commons licence and your intended use is not permitted by statutory regulation or exceeds the permitted use, you will need to obtain permission directly from the copyright holder. To view a copy of this licence, visit <http://creativecommons.org/licenses/by-nc-nd/4.0/>.

© The Author(s) 2024, corrected publication 2024